

Emergence of Tamm states from Thouless pumping

Yosuke Nakata,^{1,*} Yoshitaka Ito,¹ Yasunobu Nakamura,^{1,2} and Ryuichi Shindou^{3,4}

¹*Research Center for Advanced Science and Technology,*

The University of Tokyo, 4-6-1 Komaba, Meguro-ku, Tokyo 153-8904, Japan

²*Center for Emergent Matter Science (CEMS), RIKEN, Wako-shi, Saitama 351-0198, Japan*

³*International Center for Quantum Materials, Peking University, Beijing 100871, China*

⁴*Collaborative Innovation Center of Quantum Matter, Beijing 100871, China*

(Dated: March 19, 2019)

Localized states universally appear when a periodic potential is perturbed by defects or terminated at its surface. In one-dimensional systems, these localized states are commonly called Tamm states. In this paper, we theoretically and experimentally demonstrate a mechanism that generates Tamm states through Thouless pumping. We consider a continuous translation of the periodic potential as the pumping and prove a topological bulk–edge correspondence without relying on any symmetry protection. Based on the correspondence, we show that Tamm states emerge as topological edge states. The mechanism is experimentally verified in microwave photonic crystals.

In the 1930s, Tamm predicted the localized state of an electron near the surface of a solid [1]. Years later, Shockley explained how surface states originate from the energy levels of an isolated atom [2]. Impurities and lattice defects inside a crystal also produce similar localized states [3, 4], which play important roles in doped semiconductors. While Tamm states were first investigated for electrons, they universally appear in various wave systems. To name a few, Tamm states have been observed in electronic superlattices [5], photonic and magnetophotonic crystals [6, 7] (see also a review on photonic Tamm states [8]), plasmonic crystals [9–11], and phononic crystals [12].

The recent discovery of topological insulators has shed fresh light on the understanding of surface states from a topological perspective. In this prevalent paradigm, various topological numbers are defined under certain symmetries for periodic systems. The pioneering example is the Z_2 topological number protected by chiral symmetry, which leads to a zero-energy end state in the Su–Schrieffer–Heeger model [13, 14]. Similarly, spatial inversion symmetry quantizes the Zak phase to 0 or π [15]. The bulk–edge correspondence predicts that a boundary between two regions with different topological numbers has edge states, and the number of edge states is determined by the difference between these topological numbers. As a rigorous form of the bulk–edge correspondence for one-dimensional photonic crystals, Xiao *et al.* established a relation between the surface impedance and its bulk properties through the quantized Zak phase, which determines the existence or nonexistence of Tamm states [16]. So far, research has focused on unit cells with either chiral or inversion symmetry to define the Z_2 topological number, but these discrete symmetries may not be essential, as suggested by Shockley [2]. In fact, the in-gap Tamm states as edge states could survive under a gradual structural deformation that breaks the symmetries within the unit cell. This consideration indicates an alternative topological mechanism that generates Tamm

states without using any symmetry protection.

In this Letter, we devise a scheme that produces Tamm states from Thouless pumping. As the pumping, we consider a spatial translation of one-dimensional continuous media with a periodic potential and provide a rigorous proof of the bulk–edge correspondence without relying on any symmetry protection. The emergence of the Tamm states is experimentally demonstrated in microwave photonic crystals.

Consider a one-particle eigenmode in one-dimensional continuous media with a periodic potential of the period a . From the Bloch theorem [17], the eigenmode $|\psi_n(k)\rangle = \exp(ik\hat{x})|u_n(k)\rangle$ is characterized by the crystal momentum k in the first Brillouin zone $k \in [-\pi/a, \pi/a]$ and the energy band index n , where $\langle x|u_n(k)\rangle$ is periodic in x . We assume that there is no energy degeneracy for each energy band and focus on the n -th band. We discretize the first Brillouin zone as $k_i = i\pi/(Ma)$ for $i = -M+1, -M+2, \dots, M$ ($N = 2M$ points). In terms of $|u_i\rangle = |u_n(k_i)\rangle$, a Wilson loop is given by

$$W = \langle u_M|u_{M-1}\rangle \langle u_{M-1}|u_{M-2}\rangle \cdots \langle u_1|u_0\rangle \times \langle u_0|u_{-1}\rangle \cdots \langle u_{-M+2}|u_{-M+1}\rangle \langle u_{-M+1}|e^{iG\hat{x}}|u_M\rangle, \quad (1)$$

where $G = 2\pi/a$, and the inner product is defined in the unit cell [18]. Note that the Wilson loop W is gauge invariant, although $\exp(iG\hat{x})$ is derived from the periodic gauge. It is normalized to be unity in the thermodynamic limit $\lim_{M \rightarrow \infty} W = \exp(i\theta_{\text{Zak}})$, where the phase is simply the Zak phase [15]. The Zak phase specifies a spatial displacement of the localized Wannier orbits that are composed only of the eigenmodes in the n -th energy band [18].

Now, let us translate continuously the one-dimensional periodic potential by ξa ($0 < \xi < 1$) relative to a fixed frame of the unit cell. The spatial translation changes the potential configuration from U_0 to U_ξ inside the fixed cell [see Fig. 1(a)]. When ξ changes from 0 to 1, the localized Wannier orbit is continuously translated by the

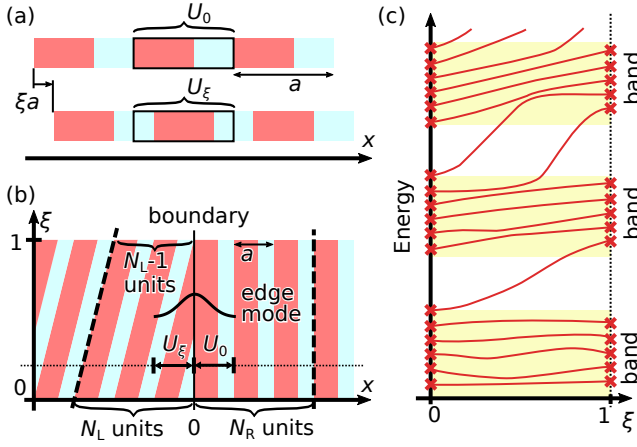


FIG. 1. (a) One-dimensional continuous medium with a periodic potential (upper) and the identical system with spatial translation by ξa (lower). (b) Spatial boundary between the two identical periodic systems with different translations. In the main text, we impose the Born-von-Karman (BvK) boundary condition, where the two dashed lines are identified with each other. (c) Eigenenergies of the whole system with the BvK boundary condition are schematically plotted as a function of the translational parameter ξ .

periodic length a . Being identical to the displacement of the Wannier orbit with the unit cell length (apart from a factor $2\pi/a$), the Zak phase also continuously increases by 2π under the translation: $\int_0^1 d\xi \partial_\xi \theta_{\text{Zak}} = 2\pi$. The phase winding counts the Chern integer defined on the (k, ξ) plane [18–20].

The 2π phase winding in the Zak phase under pumping leads to a series of non-trivial Tamm states in a spatial boundary between two identical one-dimensional periodic systems with different translations ξ . To see this, let us consider a periodic arrangement of unit cells with U_ξ in a region of $x < 0$ and another periodic arrangement of unit cells with U_0 in the other region of $x \geq 0$. The translation parameter ξ and spatial coordinate x subtend an extended two-dimensional space, as shown in Fig. 1(b). When ξ changes from 0 to 1, the Zak phase in the former bulk region ($x < 0$) winds up the 2π phase. Meanwhile, the Zak phase in the latter bulk region ($x \geq 0$) remains unchanged. Accordingly, the celebrated bulk-edge correspondence [18–20] suggests the existence of zero-dimensional edge states at the boundary region ($x = 0$), whose eigenenergies have ‘chiral’ dispersions within a bulk band gap as a function of the translational parameter ξ [Fig. 1(c)]. Moreover, as the Zak phase for *any* bulk band in the region of $x < 0$ acquires the same 2π phase winding during the translation; the number of the end states that have ‘chiral’ dispersions between the n -th and $(n+1)$ -th bulk bands are expected to be n [Fig. 1(c)].

To see this, let us impose the following Born-von-Karman (BvK) boundary condition on a finite system

[Fig. 1(b)]. Suppose that at $\xi = 0$, the whole one-dimensional system is comprised of N_L unit cells in the region of $x < 0$ and N_R unit cells in the region of $x \geq 0$. For general ξ , we identify $x = -N_L a + \xi a$ with $x = N_R a$, such that the lattice periodicity is preserved at $x = N_R a \equiv -N_L a + \xi a$ and it is broken only at $x = 0$. For $\xi = 0$ and $\xi = 1$, the periodicity is entirely preserved in the whole system, so the eigenmodes are therefore comprised of only spatially extended bulk band states. Under the BvK boundary condition, the numbers of eigenmodes in each bulk band at $\xi = 0$ and at $\xi = 1$ are $N_L + N_R$ and $N_L + N_R - 1$, respectively. Namely, the number of extended bulk states in each band decreases by one when ξ changes from 0 to 1 continuously. Since an energy is bounded from below and has no upper bound in continuous media, more than one eigenmode in each bulk band at $\xi = 0$ must move into some *higher* bands at $\xi = 1$ during the translation of ξ . For example, when one eigenmode in the lowest bulk band at $\xi = 0$ goes to the second lowest bulk band at $\xi = 1$, two eigenmodes in the second lowest bulk band at $\xi = 0$ must go to the third lowest one at $\xi = 1$ [Fig. 1(c)]. This argument inductively dictates that during the translation of ξ , n modes always raise their energies out of the n -th bulk energy band and go across the band gap between the n -th and $(n+1)$ -th bands. An in-gap mode generally has a complex-valued wavenumber [21]. Accordingly, the n in-gap modes must be spatially localized at $x = 0$, where the lattice periodicity is broken; therefore, they are simply Tamm states localized at the boundary. Importantly, the argument so far does not require any symmetry protection for the *presence* of the in-gap localized states. Note also that by tuning the translational parameter ξ , one can maximize the localization of these Tamm states [22].

Now, we confirm the theoretical idea by investigating two examples of one-dimensional photonic crystals with a finite system size (we set $N_L = N_R = 8$). The first system we studied has a unit cell with a bilayer structure [Fig. 2(a)]. The unit cell is comprised of two material regions with different lengths and permittivities. Using a transfer matrix method [22], we calculate the dispersion relation and the power transmission of the launched wave from the left vacuum region to the right. The calculated results are shown in Fig. 2(b,c). By altering ξ from 0 to 1, we observe high transmission curves transiting across the band gaps. These curves correspond to Tamm states localized around the boundary at $x = 0$, and resonant transmission occurs on the curves. For the n -th band gap, the number of moving modes is n due to the topological nature of the pumping process. In Fig. 2(d), we plot the electric-field amplitude of the narrowest localized mode with the largest imaginary part of the complex wavenumber inside the first band gap [22].

The second photonic crystal system we simulated has a trilayer structure in its unit cell. Having three different material regions, the unit cell has no spatial inversion

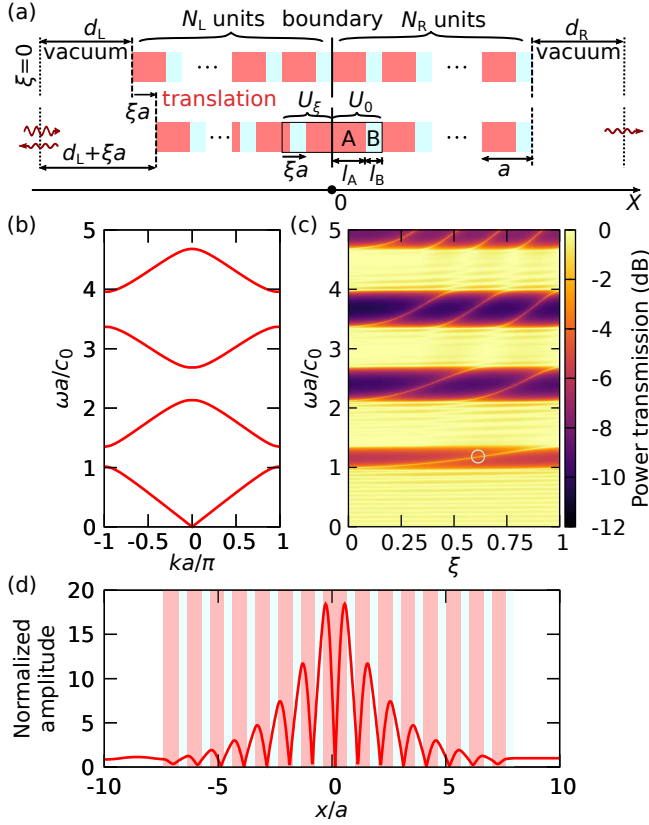


FIG. 2. (a) Configuration of a one-dimensional photonic crystal with spatial inversion symmetry and $N_L = N_R = 8$. The unit cell contains two uniform materials A and B, which have different lengths ($l_A/a = 2/3$, $l_B/a = 1/3$) and permittivities ($\epsilon_A = 10$, $\epsilon_B = 2$) and the same relative permeability ($\mu_A = \mu_B = 1$). The two extra vacuum regions are attached to the system with $d_L/a = d_R/a = 2$. Starting from a system without a defect (upper), we translate the left region ($x < 0$) by ξa (lower). (b) Dispersion relation. (c) Power transmission spectra as a function of ξ ; one can see that Tamm states transit between transmission bands. (d) Distribution of the absolute value of the complex electric-field amplitude inside the first band gap at $\xi = 0.614$ and $\omega a/c_0 = 1.18$ [depicted by the circle in (c)]. The field value is normalized by the incident wave amplitude. The speed of light in a vacuum is denoted by c_0 .

symmetry at any ξ [Fig. 3(a)]. Figs. 3(b–d) show the band structure, the power transmission spectra, and the field distribution of the Tamm state in the first band gap, respectively. The spectra show the same qualitative behavior as in the previous simulation. The results clearly demonstrate that the inversion symmetry is not essential for the generation of the series of Tamm states through the Thouless pumping.

The spatial translation of the one-dimensional photonic crystal against *any* perfect reflector [Fig. 4(a)] also gives rise to the same series of Tamm states at its boundary. To see this, let us disassemble the junction of two photonic crystals with different translation

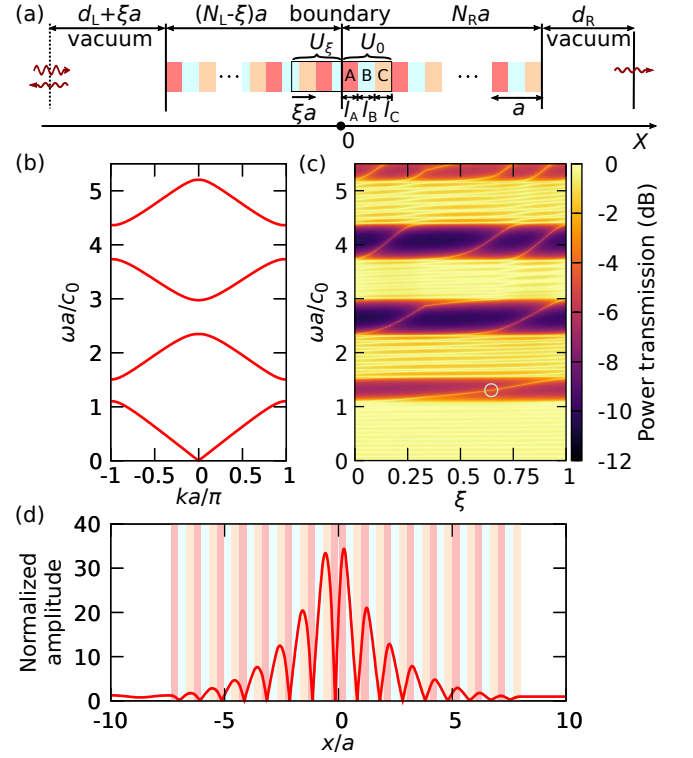


FIG. 3. (a) Configuration of a one-dimensional photonic crystal without the inversion symmetry inside the cell. The parameters are set as $l_A/a = l_B/a = l_C/a = 1/3$, $N_L = N_R = 8$, and $d_L/a = d_R/a = 2$ with $\epsilon_A = 10$, $\epsilon_B = 2$, $\epsilon_C = 6$, and $\mu_A = \mu_B = \mu_C = 1$. (b) Dispersion relation. (c) Power transmission spectra as a function of ξ . (d) Distribution of the absolute value of the complex electric-field amplitude at $\xi = 0.646$ and $\omega a/c_0 = 1.31$ [the circle in (c)].

ξ . Namely, the left region with U_ξ is now terminated at its right end by a vacuum region, while the right region with U_0 is terminated by the same vacuum region at its left end [Figs. 4(b,c)]. Photonic properties of each semi-infinite region are characterized by a complex amplitude reflection r or an effective surface impedance $Z_s \equiv (1 + r)/(1 - r)$ at the respective termination. The topological characteristics of Tamm states are encoded between the complex reflection amplitudes at both terminations $r^{(L)}(\xi, \omega)$ and $r^{(R)}(\omega)$. Specifically, a condition for localized eigenmodes in the original junction is nothing but a resonance condition across the two terminations: $Z_s^{(L)}(\xi, \omega) + Z_s^{(R)}(\omega) = 0$. The resonance condition can be also written as $r^{(L)}(\xi, \omega) \cdot r^{(R)}(\omega) = 1$. When ω stays inside a band gap between the n -th and $(n+1)$ -th bulk bands, both of the semi-infinite regions play roles of perfect reflectors: $|r^{(R)}(\omega)| = |r^{(L)}(\xi, \omega)| = 1$. Thereby, the condition shows that the phase of $r^{(L)}(\xi, \omega)$ must wind up by $2\pi n$ during the translation from $\xi = 0$ to $\xi = 1$ because the n edge modes go across the frequency ω in the gap, as in Fig. 1(c) and Fig. 2(c). Note also that the direction of the winding is determined by Foster's

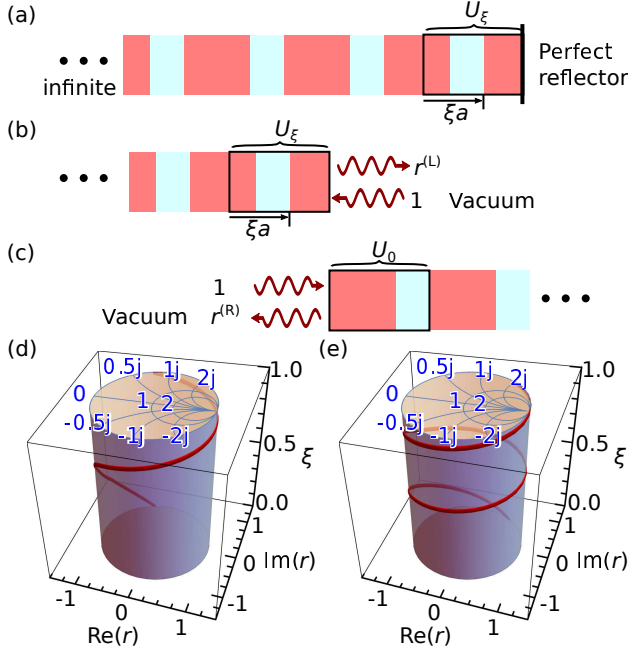


FIG. 4. (a) One-dimensional photonic crystal terminated by a perfect reflector. Definitions of (b) left and (c) right complex reflection amplitudes $r^{(L)}(\xi, \omega)$ and $r^{(R)}(\omega)$, respectively. Topological trajectories of $r^{(L)}(\xi, \omega_0)$ as a function of ξ with (d) $\omega_0 a/c_0 = 1.18$ inside the first gap and (e) $\omega_0 a/c_0 = 2.41$ inside the second gap for the system shown in Fig. 2. To read a surface impedance, the Smith chart is drawn on the top side of the cylinder.

theorem [22, 23]. As shown in Figs. 4(d,e), the transfer matrix calculation of $r^{(L)}(\xi, \omega)$ for the setup in Fig. 2 explicitly demonstrates these phase windings.

The argument so far immediately allows us to replace the right semi-infinite region with U_0 by *any* perfect reflectors. Namely, given $|r^{(R)}(\omega)| = 1$ for those ω in a gap, the phase winding of $r^{(L)}(\xi, \omega)$ during the translation of ξ from 0 to 1 always guarantees the emergence of the same number of the localized eigenmodes irrespective of details in the perfect reflector at the right side.

Finally, we experimentally confirm the theory by using periodically modulated microstrips, as depicted in Fig. 5(a). One of the fabricated samples is shown in Fig. 5(b), with the relevant parameters written in the caption. Microwaves propagate between topside metallic patterns and the backside ground plane, and the impedance and refractive index of a microstrip are determined by the geometrical parameters. Thus, two regions with different widths behave as two different media. Using a vector network analyzer (KEYSIGHT 5232A), we measured the power transmission through the samples with ξ from 0 to 1 with the step size of $\Delta\xi = 0.05$. The obtained transmission is shown in Fig. 5(c). Under 20 GHz, we clearly see five transmission bands, and four band gaps between them. The n -th band gap has n

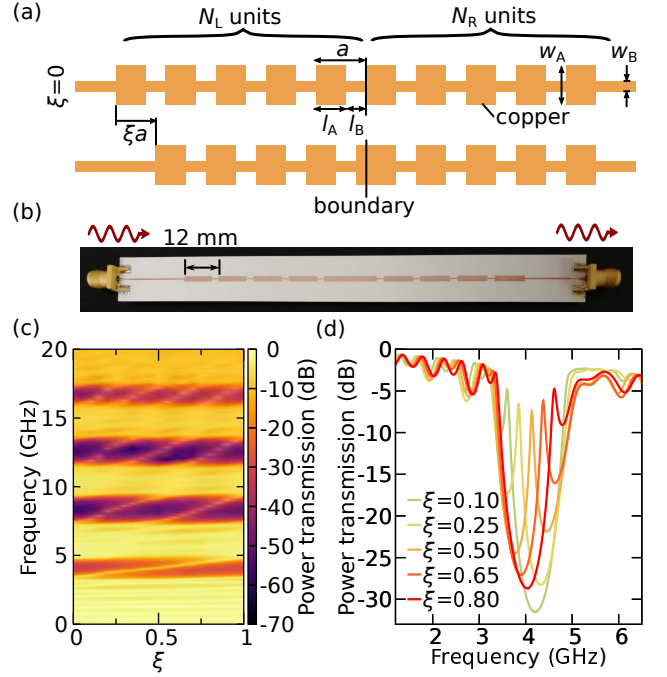


FIG. 5. (a) Schematic top view picture of microstrips (copper) at $\xi = 0$ (upper) and at $\xi \neq 0$ (lower). (b) Photograph of a sample with $\xi = 0.35$. The structural parameters are $a = 12$ mm, $l_A/a = 0.8$, $l_B/a = 0.2$, $w_A = 1.8$ mm, $w_B = 0.45$ mm, and $N_L = N_R = 5$. The microstrip is made of a 35 μm -thick copper film on a dielectric substrate (RISHO CS-3396; thickness 0.56 mm, $\epsilon = 11.3$, $\tan \delta = 0.003$ at 1 GHz), and SMA connectors (GIGALANE PSF-S01-001) are attached to the substrate. The substrate has a ground plane made of a copper film with the same thickness as the microstrip. (c) Power transmission through the 21 samples from $\xi = 0$ to $\xi = 1$ with the step size of $\Delta\xi = 0.05$. The input power is set to 0 dBm. (d) Power transmission spectra inside the first band gap for several values of ξ .

edge modes running between the two neighboring bands, as we expected from the theory. Figure 5(d) shows power transmission spectra inside the first band gap for several ξ . The transmission peak decreases and the line width becomes narrower around $\xi = 0.50$ because the coupling between the incident wave and the edge mode is reduced at the center of the band gap.

In summary, we consider a scenario that produces Tamm states through Thouless pumping. The mechanism is not restricted to a specific physical system, rather it is universal for any waves. Tamm states in a system, even without chiral or inversion symmetry, are now interpreted as topological edge modes. The termination at the spatial boundary is understood as an engineering degree of freedom and can be used for tuning the spatial localization of the Tamm states.

The authors thank K. Usami, A. Noguchi, M. W. Takeda for their fruitful discussions, and J. Koenig for his careful reading of the manuscript. This work was supported by JSPS KAKENHI (Grant

No. 17K17777) and by the JST ERATO project (Grant No. JPMJER1601). RS was supported by NBRP of China Grants No. 2014CB920901, No. 2015CB921104, and No. 2017A040215.

* nakata@qc.rcast.u-tokyo.ac.jp

- [1] I. Tamm, Phys. Z. Sowjetunion **1**, 733 (1932).
- [2] W. Shockley, Phys. Rev. **56**, 317 (1939).
- [3] H. M. James, Phys. Rev. **76**, 1611 (1949).
- [4] D. S. Saxon and R. A. Hunter, Philips Res. Rep. **4**, 81 (1949).
- [5] H. Ohno, E. E. Mendez, J. A. Brum, J. M. Hong, F. Agulló-Rueda, L. L. Chang, and L. Esaki, Phys. Rev. Lett. **64**, 2555 (1990).
- [6] P. Yeh, A. Yariv, and A. Y. Cho, Appl. Phys. Lett. **32**, 104 (1978).
- [7] T. Goto, A. V. Dorofeenko, A. M. Merzlikin, A. V. Baryshev, A. P. Vinogradov, M. Inoue, A. A. Lisyansky, and A. B. Granovsky, Phys. Rev. Lett. **101**, 113902 (2008).
- [8] A. P. Vinogradov, A. V. Dorofeenko, A. M. Merzlikin, and A. A. Lisyansky, Phys.-Usp. **53**, 243 (2010).
- [9] J. Guo, Y. Sun, Y. Zhang, H. Li, H. Jiang, and H. Chen, Phys. Rev. E **78**, 026607 (2008).
- [10] M. E. Sasin, R. P. Seisyan, M. A. Kalitchevski, S. Brand, R. A. Abram, J. M. Chamberlain, A. Y. Egorov, A. P. Vasil'ev, V. S. Mikhlin, and A. V. Kavokin, Appl. Phys. Lett. **92**, 251112 (2008).
- [11] G. C. Dyer, G. R. Aizin, S. J. Allen, A. D. Grine, D. Bethke, J. L. Reno, and E. A. Shaner, Nat. Photonics **7**, 925 (2013).
- [12] M. Xiao, G. Ma, Z. Yang, P. Sheng, Z. Q. Zhang, and C. T. Chan, Nat. Phys. **11**, 240 (2015).
- [13] W. P. Su, J. R. Schrieffer, and A. J. Heeger, Phys. Rev. Lett. **42**, 1698 (1979).
- [14] W. P. Su, J. R. Schrieffer, and A. J. Heeger, Phys. Rev. B **22**, 2099 (1980).
- [15] J. Zak, Phys. Rev. Lett. **62**, 2747 (1989).
- [16] M. Xiao, Z. Q. Zhang, and C. T. Chan, Phys. Rev. X **4**, 021017 (2014).
- [17] N. W. Ashcroft and N. D. Mermin, *Solid State Physics* (Holt, Rinehart and Winston, New York, 1976).
- [18] D. Vanderbilt, *Berry Phases in Electronic Structure Theory: Electric Polarization, Orbital Magnetization and Topological Insulators* (Cambridge University Press, Cambridge, 2018).
- [19] D. J. Thouless, Phys. Rev. B **27**, 6083 (1983).
- [20] J. K. Asbóth, L. Oroszlány, and A. Pályi, *A Short Course on Topological Insulators* (Springer, 2016).
- [21] A. A. Cottley, Am. J. Phys. **39**, 1235 (1971).
- [22] See Supplemental Material at [URL will be inserted by publisher] for detailed information of the transfer matrix methods, complex Bloch analyses and localization, and winding direction of the reflection amplitude phase.
- [23] R. E. Collin, *Foundations for microwave engineering*, 2nd ed. (McGraw-Hill, New York, 1996).

Supplemental Materials

Transfer-matrix method for one-dimensional photonic systems

To treat one-dimensional scalar wave propagation, a system is modeled by a black box with two ports with complex amplitudes a_1 , a_2 , b_1 , and b_2 , as shown in Fig. S1. The system's scattering properties are modeled by a 2×2 scattering matrix S as

$$\begin{bmatrix} b_1 \\ b_2 \end{bmatrix} = S \begin{bmatrix} a_1 \\ a_2 \end{bmatrix}. \quad (\text{S1})$$

To connect the systems, we also introduce a 2×2 transfer matrix T as

$$\begin{bmatrix} a_1 \\ b_1 \end{bmatrix} = T \begin{bmatrix} b_2 \\ a_2 \end{bmatrix}. \quad (\text{S2})$$

By multiplying these transmission matrices, we obtain a total transmission matrix. The scattering and transfer matrices are related as follows: $S_{11} = T_{21}/T_{11}$, $S_{12} = T_{22} - T_{21}T_{12}/T_{11}$, $S_{21} = 1/T_{11}$, and $S_{22} = -T_{12}/T_{11}$. Conversely, we have $T_{11} = 1/S_{21}$, $T_{12} = -S_{22}/S_{21}$, $T_{21} = S_{11}/S_{21}$, and $T_{22} = S_{12} - S_{11}S_{22}/S_{21}$.

For a one-dimensional photonic system, we can represent an electric field at a specific point as

$$\frac{E}{\sqrt{Z_0 Z_X}} = \frac{1}{\sqrt{2}}(a + b) \exp(j\omega t) + \text{c.c.}, \quad (\text{S3})$$

where we have an incoming complex amplitude a , outgoing complex amplitude b , the vacuum impedance Z_0 , and the relative impedance $Z_X = \sqrt{\mu_X/\epsilon_X}$ with relative permittivity ϵ_X and relative permeability μ_X at the point in a material X . Note that we use $j = -i$ for a photonic system, and Im represents the coefficient of the imaginary part of j . At the boundary between two regions with material X (left) and Y (right), we have the following scattering matrix:

$$S_{XY}^b = \frac{1}{Z_X + Z_Y} \begin{bmatrix} Z_Y - Z_X & 2\sqrt{Z_X Z_Y} \\ 2\sqrt{Z_X Z_Y} & Z_X - Z_Y \end{bmatrix}. \quad (\text{S4})$$

Correspondingly, we have T_{XY}^b as the transfer matrix for S_{XY}^b . For free propagation across a length l in X , we have the following transfer matrix:

$$T_X^f(\omega) = \begin{bmatrix} \exp(jk_X l) & 0 \\ 0 & \exp(-jk_X l) \end{bmatrix}, \quad (\text{S5})$$

with wavenumber $k_X = \omega/c_X$ and speed of light c_X in X . By using a refractive index $n_X = \sqrt{\epsilon_X \mu_X}$ in X , c_X is written as c_0/n_X , with the speed of light c_0 in a vacuum.

Now, we consider a unit cell of a photonic crystal with a length l_i of a material X_i from left to right ($i = 1, 2, \dots, M$). The transfer matrix of the unit cell is defined as

$$T^{\text{unit}}(\omega) = T_{X_M X_1}^b T_{X_1}^f(\omega) \prod_{i=2}^M T_{X_{i-1} X_i}^b T_{X_i}^f(\omega). \quad (\text{S6})$$

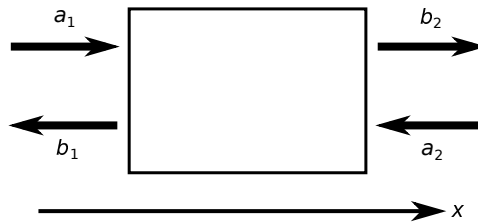


FIG. S1. Model of two-port system.

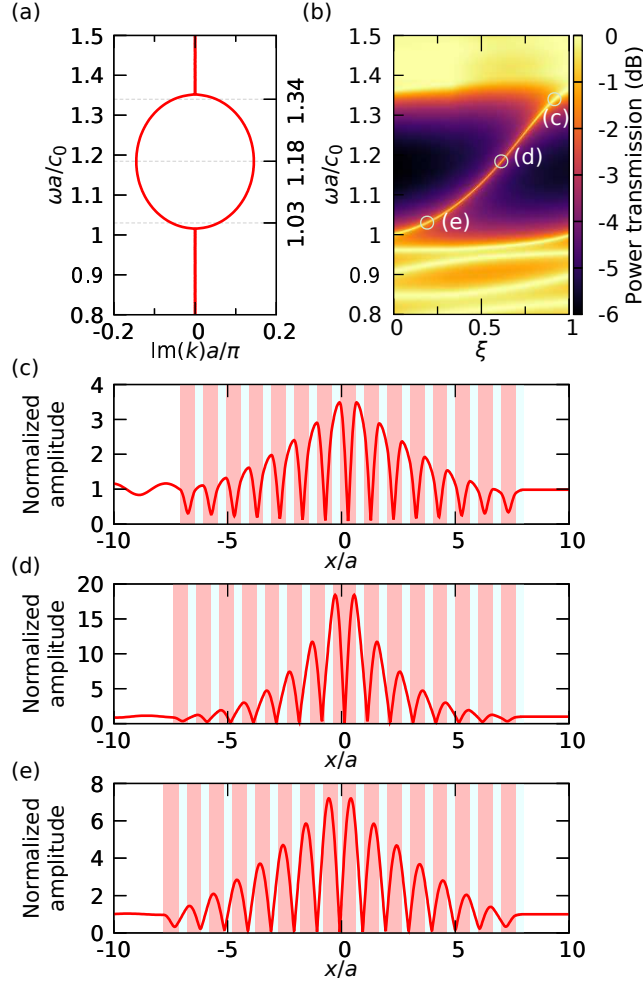


FIG. S2. Details of the first band gap of the system shown in Fig. 2 of the main text. (a) Imaginary part of the complex wavenumber. (b) Power transmission spectra. Distribution of the absolute value of the complex electric-field amplitude for (c) $(\xi, \omega a/c_0) = (0.190, 1.03)$, (d) $(0.614, 1.18)$, and (e) $(0.916, 1.34)$. These points are also indicated in (b) by circles. The field values are normalized by the incident wave amplitude.

Eigenvalues of $T^{\text{unit}}(\omega)$ are given by $\exp(jka)$ with the complex Bloch wavenumber k and the unit cell length $a = \sum_i l_i$. From an eigenvector $\mathbf{v} = [v_1 \ v_2]^T$ with $\text{Im}(k) > 0$ (decaying to left) for $T^{\text{unit}}(\omega)$ inside a band gap, we can calculate $r^{(L)} = w_1/w_2$ by using $\mathbf{w} = [w_1 \ w_2]^T = (T_{X_M V}^b)^{-1} \mathbf{v}$ with a vacuum V for the setup shown in Fig. 4(b) of the main text.

To obtain the power transmission, we calculate a total transmission matrix T^{tot} for the whole system, and then obtain the scattering matrix S^{tot} . Then, we have the power transmission $|S_{21}^{\text{tot}}|^2$ for an incident wave from the left. Multiplying a series of transfer matrices to $\mathbf{v}_{\text{out}} = [S_{21}^{\text{tot}} \ 0]^T$, we obtain the electric-field distribution.

Complex Bloch analysis and localization

In this part, we compare some edge modes inside the first gap shown in Fig. 2 of the main text. Generally, we have complex wavenumbers inside band gaps. Figure S2(a) shows the imaginary part of the complex wavenumber inside the first band gap for the model. Around the center region of the band gap, the imaginary part is maximized. Figure S2(b) shows the power transmission, which is enlarged from Fig. 2(c) in the main text. To see the variation of the distribution, we took three points along the edge-mode dispersion depicted as circles in Fig. S2(b). The corresponding field distributions are plotted in Figs. S2(c-e). As we expected from Fig. S2(a), localization is the narrowest in the center of the band gap. Thus, we can tune localization by altering ξ , i.e., the termination. The narrowest localization decreases the coupling to the incident wave, and the radiative loss is reduced more effectively.

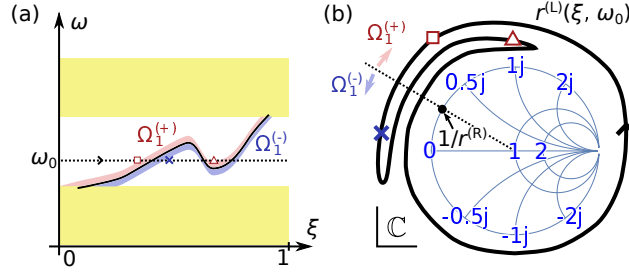


FIG. S3. (a) Possible situation for an edge-mode transition for the first band gap. (b) Corresponding trajectory of $r^{(L)}(\xi, \omega_0)$ from $\xi = 0$ to 1, while fixing $\omega = \omega_0$.

Therefore, the field amplitude of Fig. S2(d) becomes higher than those of Figs. S2(c) and (e). Thus, we can control the radiative coupling by changing ξ .

Winding direction of reflection amplitude

Based on Foster's theorem, we determine the rotation direction of $r^{(L)}(\xi, \omega_0)$ from $\xi = 0$ to $\xi = 1$ for ω_0 inside a band gap. In this section, we concentrate on the band gap between the n -th and $(n+1)$ -th bands. Thus, we have n edge modes, and their eigenfrequencies $\omega = \omega_i(\xi)$ ($i = 1, 2, \dots, n$) are determined by $r^{(L)}(\xi, \omega) \cdot r^{(R)}(\omega) = 1$, where $\omega_i(0)$ and $\omega_i(1)$ are inside the n -th band and the $(n+1)$ -th band, respectively. We define the following regions: $\Omega_i^{(+)} = \{(\xi, \omega) | \xi \in [0, 1], \omega_i(\xi) < \omega < \omega_i(\xi) + \Delta\omega\}$ and $\Omega_i^{(-)} = \{(\xi, \omega) | \xi \in [0, 1], \omega_i(\xi) - \Delta\omega < \omega < \omega_i(\xi)\}$, with a small $\Delta\omega > 0$. A possible situation for $n = 1$ is graphically shown in Fig. S3. We assume that the system is passive. Thus, Foster's reactance theorem can be applied [23]. Then, $r^{(L)}(\xi, \omega) \cdot r^{(R)}(\omega)$ must *monotonically* rotate *clockwise* in the complex plane when we increase ω . Therefore, we have $\arg r^{(L)} < -\arg r^{(R)}$ and $\arg r^{(L)} > -\arg r^{(R)}$ for $\Omega_i^{(+)}$ and $\Omega_i^{(-)}$, respectively. Now, consider $r^{(L)}(\xi, \omega_0)$, with a specified ω_0 inside the band gap. By changing ξ from 0 to 1 along $\omega = \omega_0$, the numbers of transitions from $\Omega_i^{(+)}$ to $\Omega_i^{(-)}$ ($\Omega_i^{(-)}$ to $\Omega_i^{(+)}$) are denoted by m_i° (m_i°), respectively. From the topological behavior of $\omega_i(\xi)$, we have $m_i^{\circ} - m_i^{\circ} = 1$. In the Smith chart, $\Omega_i^{(+)} \rightarrow \Omega_i^{(-)}$ corresponds to the situation that $r^{(L)}$ crosses over $[r^{(R)}(\omega_0)]^{-1}$ in an anti-clockwise manner. Similarly, $\Omega_i^{(-)} \rightarrow \Omega_i^{(+)}$ represents clockwise crossing. Then, the winding number in the Smith chart must be n in an anti-clockwise manner with changing ξ from 0 to 1 because the trajectory is continuous.